

Dynamical magnetic fields in heavy-ion collisions

Anping Huang,^{1,2} Duan She,^{3,4} Shuzhe Shi,⁵ Mei Huang,^{1,*} and Jinfeng Liao^{2,†}

¹*School of Nuclear Science and Technology, University of Chinese Academy of Sciences, Beijing 100049, China*

²*Physics Department and Center for Exploration of Energy and Matter,*

Indiana University, 2401 N Milo B. Sampson Lane, Bloomington, Indiana 47408, USA

³*Department of Modern Physics, University of Science and Technology of China, Anhui 230026, China*

⁴*Key Laboratory of Quark and Lepton Physics (MOE),*

Central China Normal University, Wuhan 430079, China

⁵*Department of Physics and Astronomy, Stony Brook University, Stony Brook, New York 11794-3800, USA*

(Dated: December 19, 2022)

The magnetic fields in heavy-ion collisions are important ingredients for many interesting phenomena, such as the Chiral Magnetic Effect, Chiral Magnetic Wave, the directed flow v_1 of D^0 mesons and the splitting of the spin polarization of the $\Lambda/\bar{\Lambda}$. Quantitative studies of these phenomena however suffer from limited understanding on the dynamical evolution of these fields in the medium created by the collisions, which remains a critical and challenging problem. The initial magnetic fields from the colliding nuclei decay very fast in the vacuum but their lifetime could be extended through medium response due to electrically conducting quarks and antiquarks. Here we perform a detailed analysis of such medium effect on the dynamical magnetic fields by numerically solving the Maxwell's equations concurrently with the expanding medium described by viscous hydrodynamics, under the assumption of negligible back reaction of the fields on the fluid evolution. Our results suggest a considerable enhancement of late time magnetic fields, the magnitude of which depends sensitively on the fireball expansion as well as the medium electric conductivity both before and during hydrodynamic stage.

I. INTRODUCTION

The ultra-relativistic heavy-ion collisions provide the opportunity to create quark-gluon plasma (QGP) and investigate its properties under extreme conditions in terms of temperatures, baryon densities, and more recently also magnetic fields and vorticity. There are very strong magnetic fields arising from the fast-moving ions in the non-central heavy-ion collisions, which can reach about $eB \sim m_\pi^2 \sim 10^{18}$ Gauss in Au+Au collisions at the Relativistic Heavy Ion Collider (RHIC), and can be still an order of magnitude larger at the Larger Hadron Collider (LHC) [1–8]. Many interesting effects induced by such magnetic fields have been proposed and studied both theoretically and experimentally, such as the Chiral Magnetic Effect, Chiral Magnetic Wave, the directed flow v_1 of D^0 mesons and the splitting of the spin polarization of the $\Lambda/\bar{\Lambda}$, etc. See recent reviews in e.g. [9–15].

While the initial strength and spatial distribution of the magnetic fields at the beginning of a heavy ion collision can be accurately calculated, the subsequent dynamical evolution of such magnetic fields in the medium is rather poorly determined. If one only considers the field evolution in vacuum case, it is well known that the strength decays rapidly in time and the field lifetime at mid-rapidity can be estimated as $\tau_B \sim R_A/(\gamma v_z)$ which is about 0.06 fm for Au+Au collision at 200 GeV [15] while about 0.005 fm for Pb+Pb collisions at 2.76 TeV. However, the lifetime of the in-medium magnetic field

could be elongated due to the presence of the quark-gluon plasma in which the electrically charged quarks and antiquarks form a conducting medium with induction effect, as qualitatively demonstrated by various theoretical and numerical investigations [16–29]. A quantitative understanding of the dynamical evolution of magnetic fields, however, remains a key challenge.

Generally speaking, there are two different types of approaches, the “strong field” and “weak field” methods. In the strong field method, the influence of the electromagnetic fields on the medium evolution can not be ignored and thus need to be taken into account for describing the medium. The most representative example is the Magneto-hydrodynamics (MHD). In an ideal MHD with infinite conductivity, the magnetic field obeys the frozen flux (or Alfven) theorem and can therefore be represented simply in time [30, 31] for a Bjorken flow, i.e. $B(\tau) = B_0 \tau_0/\tau$, where B_0 is the initial magnetic field at time τ_0 . Numerical efforts were developed in [32, 33] by using the improved version of ECHO-QGP to simulate the evolution of electromagnetic fields in the heavy-ion collisions by solving the relativistic ideal MHD equations with the assumption of infinite electrical conductivity of the plasma and the ideal hydro for the medium without the dissipative effects. These analyses show that the medium effect would indeed slow down the decay of the magnetic field and hence enlarge its lifetime. However, given the strongly coupled nature of the quark-gluon plasma, it is difficult to imagine that the electric conductivity would be very large. In fact, lattice simulations would suggest a rather limited QGP electric conductivity.

In the weak field method, one assumes that the ef-

* huangmei@ucas.ac.cn

† liaoji@indiana.edu

fect of the medium on electromagnetic fields must be accounted for while the back reaction of electromagnetic fields on the medium is negligible. In this approach, the medium evolution can be described by usual viscous hydrodynamics without electromagnetic fields and the evolution of the electromagnetic fields can be derived from the Maxwell's equations by including the responses from the medium via e.g. induction currents. Several previous theoretical and numerical works adopted this method, see e.g. [7, 8, 34–38]. These studies also clearly demonstrated the medium response effect that can help extend the lifetime of magnetic fields, but often suffer from various unrealistic approximations e.g. constant conductivity, static medium, 1D Bjorken expansion only, infinite transverse medium, etc.

Quantitatively understanding the dynamical evolution of magnetic fields requires a more realistic hydrodynamic background, a more realistic QGP conductivity, a proper treatment of the full spacetime dependence of the fields, as well as a careful analysis of the per-hydro non-equilibrium stage. In this work, we make an attempt at address these issues based on the weak field method through numerically solving concurrently the viscous hydrodynamics for the medium and the Maxwell's equations for the electromagnetic fields. To be specific, let's take the $\sqrt{s_{NN}} = 200$ GeV Au+Au collisions as an example to demonstrate the developed framework. The full evolution includes three different stages in our framework. The first stage is the initial stage of time interval $\tau = 0.0 \sim 0.1$ fm, which may be gluon dominated with few quarks. At this time there would be no medium response and the electromagnetic fields are assumed to evolve in vacuum. The second stage is the pre-equilibrium stage of time interval $\tau = 0.1 \sim 0.4$ fm where the system is undergoing Bjorken expansion. While substantial number of quarks and antiquarks emerge in this stage, they may or may not be close to thermal equilibrium yet. Since there is no clear answer for the electric conductivity in such non-equilibrium case, we will test several plausible assumptions for the pre-equilibrium effective electric conductivity, such as the zero model, constant model and linear model. The third stage is the hydrodynamic stage for time $\tau \geq 0.4$ fm, in which the QGP medium is assumed to have thermal conductivity and several scenarios for the conductivity will also be tested. A more detailed description of our framework will be presented later.

The rest of this paper is organized as follows. In Sec. II, the analytical solution and the numerical algorithm of Maxwell's equations in the static QGP scenario are briefly reviewed, with certain new results for dynamic magnetic fields under static QGP with space-time-dependent conductivity. In Sec. III, the dynamical evolution of magnetic fields in dynamically expanding QGP is studied and the results are compared for different models of both thermal and pre-equilibrium conductivities as well as for different choices of hydrodynamic backgrounds. Finally we conclude in Sec. IV. A number

of relevant technical details are also included in several appendices: Appendix A presents the external electric and magnetic fields in heavy-ion collision as solutions of Eq. (11); Appendix B introduces the Yee-grid algorithm for solving the Maxwell's equations; Appendix C briefly reviews the Levi-Civita tensor and electromagnetic tensor in Milne space used for the expanding case; Appendix D discusses the difference of the velocity in Milne space and Minkowski space.

II. DYNAMICAL MAGNETIC FIELD IN A STATIC QGP

The covariant Maxwell equations are

$$\begin{aligned}\partial_\mu F^{\mu\nu} &= J^\nu, \\ \partial_\mu \tilde{F}^{\mu\nu} &= 0,\end{aligned}\tag{1}$$

where $\tilde{F}^{\mu\nu} = \frac{1}{2}\epsilon^{\mu\nu\alpha\beta}F_{\alpha\beta}$ is a dual tensor of the electromagnetic field tensor $F^{\mu\nu} = \partial^\mu A^\nu - \partial^\nu A^\mu$. Using the relations $B^i = -\frac{1}{2}\epsilon^{ijk}F_{jk} = \tilde{F}^{i0}$, $E^i = F^{i0}$, $F^{ij} = \epsilon^{ijk}B_k$, the covariant Maxwell equations (1) can be rewritten as the familiar form,

$$\begin{aligned}\nabla \cdot \mathbf{E} &= J^0, \\ \nabla \cdot \mathbf{B} &= 0, \\ \partial_t \mathbf{E} &= \nabla \times \mathbf{B} - \mathbf{J}, \\ \partial_t \mathbf{B} &= -\nabla \times \mathbf{E}.\end{aligned}\tag{2}$$

The first two equations are the constraint equations, while the last two equations the dynamical equations of the electromagnetic fields. The latter can be used to derive the electric and magnetic fields at next time step. In a static medium, the current J^0 and \mathbf{J} can expanded as the following,

$$J^0 = J_s^0, \quad \mathbf{J} = \sigma \mathbf{E} + \sigma_\chi \mathbf{B} + \mathbf{J}_s,\tag{3}$$

with σ and σ_χ respectively being the electric and chiral conductivities of QGP. J_s^0 and \mathbf{J}_s are the source contributions from the fast moving protons in the colliding nuclei. They can be written as

$$J_s^0 = e \sum_i \delta(\mathbf{x}_\perp - \mathbf{x}'_{\perp,i}) \delta(z - z'_i - \beta t),\tag{4}$$

$$\mathbf{J}_s = e \sum_i \beta \hat{z} \delta(\mathbf{x}_\perp - \mathbf{x}'_{\perp,i}) \delta(z - z'_i - \beta t).\tag{5}$$

From the above Maxwell equations (2), we can construct the corresponding wave equations for the electric and magnetic fields,

$$\begin{aligned}(\nabla^2 - \partial_t^2 - \sigma \partial_t) \mathbf{E} - \sigma_t \mathbf{E} + \sigma_\chi \nabla \times \mathbf{E} \\ = \sigma_{\chi,t} \mathbf{B} + \partial_t \mathbf{J}_s + \nabla J_s^0,\end{aligned}\tag{6}$$

$$\begin{aligned}(\nabla^2 - \partial_t^2 - \sigma \partial_t) \mathbf{B} + (\nabla \sigma_\chi) \times \mathbf{B} + \sigma_\chi \nabla \times \mathbf{B} \\ = -(\nabla \sigma) \times \mathbf{E} - \nabla \times \mathbf{J}_s,\end{aligned}$$

where we have used the notations $\sigma_t = \partial_t \sigma$, $\sigma_{\chi,t} = \partial_t \sigma_\chi$.

A. analytical solution of Maxwell Equations at constant conductivities

It is possible to analytically solve the Maxwell equations Eq. (2) or Eq. (6), when the electric and chiral conductivity are all constant for space-time [34–36]. In such a case, the wave equation (6) can be simplified as

$$\begin{aligned} (\nabla^2 - \partial_t^2 - \sigma \partial_t) \mathbf{E} + \sigma_\chi \nabla \times \mathbf{E} &= \partial_t \mathbf{J}_s + \nabla J_s^0, \\ (\nabla^2 - \partial_t^2 - \sigma \partial_t) \mathbf{B} + \sigma_\chi \nabla \times \mathbf{B} &= -\nabla \times \mathbf{J}_s. \end{aligned} \quad (7)$$

Adopting the cylindric coordinate, its analytical solution is found to be [34–36]

$$\begin{aligned} B_\phi &= \frac{Q}{4\pi} \frac{v\gamma x_T}{\Delta^{3/2}} \left(1 + \frac{\sigma v\gamma}{2} \sqrt{\Delta}\right) e^A, \\ B_r &= -\sigma_\chi \frac{Q}{8\pi} \frac{v\gamma^2 x_T}{\Delta^{3/2}} \left[\gamma(vt - z) + A\sqrt{\Delta}\right] e^A, \\ B_z &= \sigma_\chi \frac{Q}{8\pi} \frac{v\gamma}{\Delta^{3/2}} \left[\gamma^2(vt - z)^2 \left(1 + \frac{\sigma v\gamma}{2} \sqrt{\Delta}\right) \right. \\ &\quad \left. + \Delta \left(1 - \frac{\sigma v\gamma}{2} \sqrt{\Delta}\right)\right] e^A, \end{aligned} \quad (8)$$

$$\begin{aligned} E_\phi &= \sigma_\chi \frac{Q}{8\pi} \frac{v^2 \gamma^2 x_T}{\Delta^{3/2}} \left[\gamma(vt - z) + A\sqrt{\Delta}\right] e^A, \\ E_r &= \frac{Q}{4\pi} \left\{ \frac{\gamma x_T}{\Delta^{3/2}} \left(1 + \frac{\sigma v\gamma}{2} \sqrt{\Delta}\right) \right. \\ &\quad \left. - \frac{\sigma}{vx_T} e^{-\sigma(t-z/v)} \left[1 + \frac{\gamma(vt - z)}{\sqrt{\Delta}}\right] \right\} e^A, \\ E_z &= \frac{Q}{4\pi} \left\{ -e^A \frac{1}{\Delta^{3/2}} \left[\gamma(vt - z) + A\sqrt{\Delta} + \frac{\sigma\gamma}{v} \Delta\right] \right. \\ &\quad \left. + \frac{\sigma^2}{v^2} e^{-\sigma(t-z/v)} \Gamma(0, -A) \right\}, \end{aligned} \quad (9)$$

where $\Delta \equiv \gamma^2(vt - z)^2 + x_T^2$, $A \equiv (\sigma v\gamma/2)[\gamma(vt - z) - \sqrt{\Delta}]$, $\Gamma(0, -A)$ is the incomplete gamma function defined as $\Gamma(a, z) = \int_z^\infty dt t^{a-1} e^{-t}$.

As noted above, such an analytical solution is based on the precondition that the electric and chiral conductivities are space-time independent. Such a condition is not satisfied by the rapidly expanding medium form in the heavy-ion collision. It seems unrealistic to analytically solve the wave equations Eq. (6) or the Maxwell equations Eq. (2) when the conductivities are space-time dependent. To further investigate the realistic dynamical evolution of the electromagnetic field in heavy-ion collisions, it calls for the numerical calculations.

B. numerical method to solve Maxwell Equations

Numerically solving the Maxwell equations in Eq. (2) might be unstable, due to the Dirac delta functions in the source term. Therefore, we will adopt the method established by McLerran and Skokov [7]. In this method,

the electric and magnetic fields are separated into two pieces, i.e

$$\mathbf{E} = \mathbf{E}_{ext} + \mathbf{E}_{int}, \quad \mathbf{B} = \mathbf{B}_{ext} + \mathbf{B}_{int}. \quad (10)$$

The subscript “ext” denotes the external part which originated by the source contribution from the fast moving charge particles in heavy-ion collisions, whereas “int” refers to the induced electromagnetic fields generated in the created quark-gluon plasma (QGP). Then the Maxwell equations in Eq. (2) under static medium now can be split into two parts. For the “external” part,

$$\begin{aligned} \nabla \cdot \mathbf{E}_{ext} &= J_s^0, \\ \partial_t \mathbf{E}_{ext} &= \nabla \times \mathbf{B}_{ext} - \mathbf{J}_s, \\ \nabla \cdot \mathbf{B}_{ext} &= 0, \\ \partial_t \mathbf{B}_{ext} &= -\nabla \times \mathbf{E}_{ext}. \end{aligned} \quad (11)$$

There is analytical solution to this set of equations, which is the electric and magnetic fields induced by the fast moving charged particles. Details can be found in Appendix A. The “internal” part is,

$$\begin{aligned} \nabla \cdot \mathbf{E}_{int} &= 0, \\ \partial_t \mathbf{E}_{int} &= \nabla \times \mathbf{B}_{int} - \sigma(\mathbf{E}_{int} + \mathbf{E}_{ext}) - \sigma_\chi(\mathbf{B}_{int} + \mathbf{B}_{ext}), \\ \nabla \cdot \mathbf{B}_{int} &= 0, \\ \partial_t \mathbf{B}_{int} &= -\nabla \times \mathbf{E}_{int}. \end{aligned} \quad (12)$$

We numerically solve this equation set to obtain the internal electric and magnetic fields in the medium at any time, and then resulting the dynamical electric and magnetic field in heavy-ion collisions is obtained by adding the external and internal parts.

For numerical stability for the conductivity ranging from 0 to ∞ when solving Eq. (12), we chose the Yee’s algorithm [39] which belongs to the category of Leapfrog algorithms. In Yee’s algorithm, the computed fields \mathbf{E} and \mathbf{B} are staggered by half a step in space-time with respect to each other. More details about the algorithm of Eq. (12) is presented in Appendix B. The code package of this section is publicly available at <https://github.com/brangja/EB-in-HIC.git>.

C. numerical results

In this subsection, we present the numerical results with the aforementioned numerical method. The simulation is performed using initial condition of the electromagnetic field provided by event-averaged MC-Glauber simulation for Au+Au collisions at RHIC energy $\sqrt{s_{NN}} = 200$ GeV and impact parameter $b = 6$ fm. The velocity and Lorentz factor for both target and projectile can be estimated by $v^2 = 1 - \gamma^{-2}$ and $\gamma = \sqrt{s_{NN}}/2m_p$. To explore the effect of conductivity, we parametrize the electric conductivity as the result of hot QCD medium is

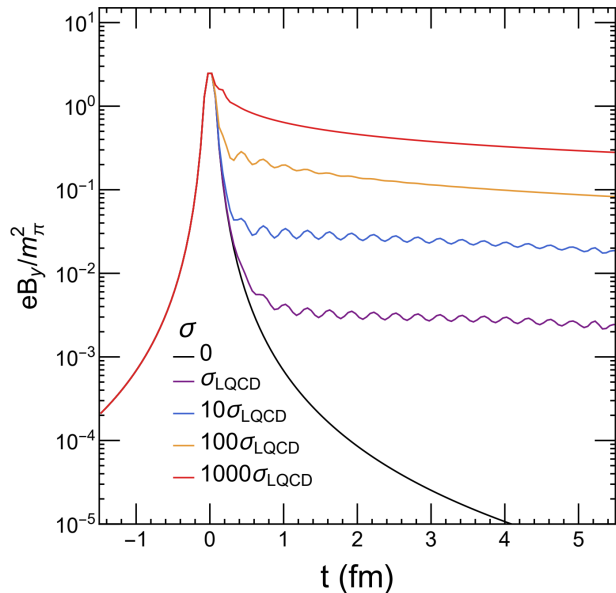


FIG. 1. The dynamical magnetic field in the static medium.

obtained in the lattice calculations [18] scaled by a factor (λ),

$$\sigma = \lambda \sigma_{\text{LQCD}} = 5.8 \lambda \text{ MeV}. \quad (13)$$

To test the stability of our program and investigate influence of the conductivity on the evolution of the magnetic field, the parameter is chosen as $\lambda = 1, 10, 100$, and 1000 . The chiral conductivity is [40]

$$\sigma_\chi = \left(\frac{e^2}{2\pi^2} N_c \sum_f q_f^2 \right) \mu_5, \quad (14)$$

where μ_5 is the chiral chemical potential. Based on these inputs and the aforementioned method, we numerically solve the time evolution of the magnetic field in the origin $\mathbf{x} = 0$ as a function of the electric conductivity. Results are shown in Fig. 1, which are qualitatively consistent with McLerran and Skokov [7]¹. In our calculation, we took two values of the chiral chemical potential, an optimistic limit that $\mu_5 = 1$ GeV and a pessimistic limit that $\mu_5 = 0$. We find the difference between these two cases to be negligible.

The rapidly expanding conducting medium created in heavy-ion collisions is highly inhomogeneous. A realistic simulation requires a space-time dependent electric conductivity. Meanwhile, quarks are not formed immediately after the initial collisions, and it takes finite time for the quark to equilibrate. One needs to pay special

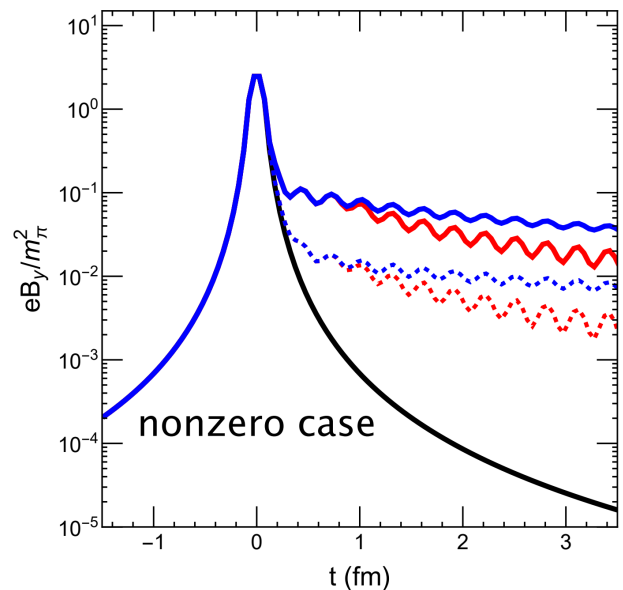
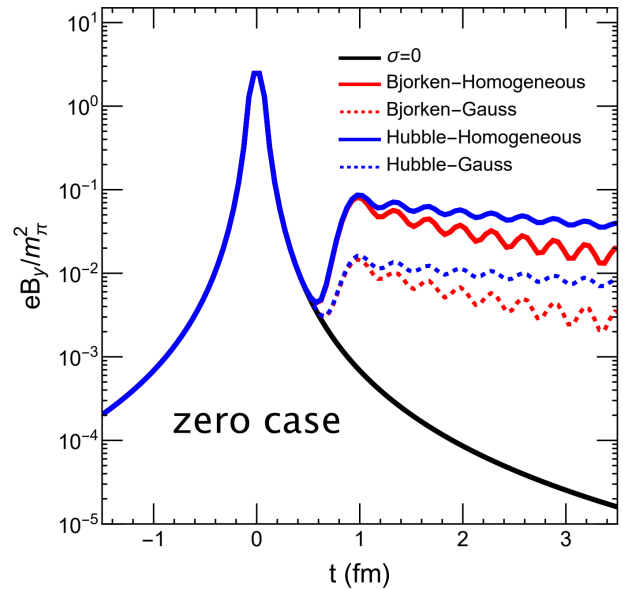


FIG. 2. Time dependence of the magnetic field along the out-of-plane direction. Upper and lower panels compare the effect of pre-equilibrium conductivity (17). In each plot, red and blue lines compare the temporal distribution (15), whereas solid and dashed lines compare the spatial distribution (16).

attention to the non-trivial time dependence of σ in the pre-equilibrium stage.

Herein, we test the influence of different components by choosing a couple of different models in the simulation. To explore the limits without transverse expansion and with the strongest one, we take two the Bjorken and Hubble models to estimate the time-dependent of electric

¹ We speculate the difference in qualitative value to be due to the fact that a different colliding system was considered in [7]. See also [37].

conductivity, $\sigma(t)$, i.e.,

$$\begin{aligned} \text{Bjorken:} \quad \sigma(t) &= \sigma_c \frac{T(t)}{T_c} = \sigma_c \frac{T_0}{T_c} \left(\frac{t_0}{t} \right), \\ \text{Hubble:} \quad \sigma(t) &= \sigma_c \frac{T(t)}{T_c} = \sigma_c \frac{T_0}{T_c} \left(\frac{t_0}{t} \right)^{\frac{1}{3}}. \end{aligned} \quad (15)$$

In our calculation, we take $T_0 = 3T_c$ and $\sigma_c = 10\sigma_{\text{LQCD}}$. The spacial dependent is then modeled by assuming homogeneous or Gaussian profile,

$$\begin{aligned} \text{Homogeneous:} \quad \sigma(t, \mathbf{x}) &= \sigma(t), \\ \text{Gaussian:} \quad \sigma(t, \mathbf{x}) &= \sigma(t) e^{-\frac{x^2}{R_x^2} - \frac{y^2}{R_y^2} - \frac{z^2}{R_z^2}}, \end{aligned} \quad (16)$$

where the corresponding parameters at the Gaussian model are $R_x = R_A - b/2$, $R_y = \sqrt{R_A^2 - b^2}/4$, $R_z = 3$ fm, $R_A = 6.38$ fm the radius of Au, $b = 6$ fm the impact parameter. Finally, the effect of quark formation time is estimated by taking two limits — quarks at time $0 \leq t \leq t_0$ are not created at all, or rapidly created to its density at t_0 . Correspondingly, the conductivity is parametrized as

$$\begin{aligned} \text{zero:} \quad & \begin{cases} \sigma(t) = 0, & t \leq t_0, \\ \sigma(t) \neq 0, & t_0 < t; \end{cases} \\ \text{non-zero:} \quad & \begin{cases} \sigma(t) = 0, & t \leq 0, \\ \sigma(t) = \sigma(t_0), & 0 < t \leq t_0, \\ \sigma(t) \neq 0, & t_0 < t. \end{cases} \end{aligned} \quad (17)$$

Here the $t_0 = 0.4$ fm is the start time of the hydro stage which is assumed as global equilibrium. The picture of these two cases is that the system is under the pre-equilibrium stage at time interval $0 < t < t_0$, and then the system is close to the equilibrium stage after time $t = t_0$. the difference is on the conductivity at the pre-equilibrium stage. Corresponding numerical results are showed in Fig. 2. It shows that the $B(t)$ is very sensitive to the effective conductivity of the pre-equilibrium stage ($0 < t < t_0$) and the hydro stage ($t \geq t_0$).

III. DYNAMICAL MAGNETIC FIELDS IN THE NON-STATIC QGP

A. the Maxwell equation in Milne space

It is convenient to work on the Milne space for investigating the dynamic evolution of the electromagnetic field in the rapidly expanding QGP. The Maxwell equation can be expressed as

$$\hat{D}_\mu F_M^{\mu\nu} = J^\nu, \quad (18)$$

$$\hat{D}_\mu \tilde{F}_M^{\mu\nu} = 0, \quad (19)$$

where the electromagnetic field tensor is marked with the subscript M to refer to Milne coordinate. The covariant

derivative \hat{D}_μ acting on a tensor is expressed as $\hat{D}_\mu t^{\nu\rho} = \partial_\mu t^{\nu\rho} + \Gamma_{\lambda\mu}^\nu t^{\lambda\rho} + \Gamma_{\lambda\mu}^\rho t^{\nu\lambda}$, with affine connections $\Gamma_{\mu\nu}^\rho = (1/2)g^{\rho\sigma}(\partial_\nu g_{\sigma\mu} + \partial_\mu g_{\sigma\nu} - \partial_\sigma g_{\mu\nu})$. We adopt the metric convention to be $g_{\mu\nu} = \text{diag}(1, -1, -1, -\tau^2)$. The dual tensor is $\tilde{F}_M^{\mu\nu} = (1/2)\epsilon^{\mu\nu\rho\sigma} F_{\rho\sigma}^M$. Herein, the Levi-Civita tensor $\epsilon^{\mu\nu\rho\sigma}$ and the electromagnetic tensor are different from the case of Minkowski coordinate, and their explicit forms can be found in Appendix C. The currents are composed of normal currents, diffusion current, Ohm's law, and CME current as the following,

$$\begin{aligned} J^\mu &= J_{in}^\mu + J_s^\mu, \\ J_{in}^\mu &= n u^\mu + d^\mu + \sigma F_M^{\mu\nu} u_\nu + \sigma_\chi \tilde{F}_M^{\mu\nu} u_\nu. \end{aligned} \quad (20)$$

Herein, J_{in}^μ denotes the current in the medium, and J_s^μ the source contributions from the fast moving charged particles in heavy-ion collisions, n is the charge number density and d^μ the diffusive current. We further denote electric and magnetic fields in the Milne space as

$$\tilde{E}^i = F_M^{i0}, \quad \tilde{B}^i = \tilde{F}_M^{i0}, \quad (21)$$

with i being x, y , or η . The current in the medium can be further simplified as follows,

$$\begin{aligned} J_{in}^\mu &= (J^\tau, J^x, J^y, J^\eta), \\ J^\tau &= n u^\tau + d^\tau + \sigma \left(\tilde{E}^x u^x + \tilde{E}^y u^y + \tau^2 \tilde{E}^\eta u^\eta \right) \\ &\quad + \sigma_\chi \left(\tilde{B}^x u^x + \tilde{B}^y u^y + \tau^2 \tilde{B}^\eta u^\eta \right), \\ J^x &= n u^x + d^x + \sigma \left(\tilde{E}^x u^\tau + \tau \tilde{B}^\eta u^y - \tau \tilde{B}^y u^\eta \right) \\ &\quad + \sigma_\chi \left(\tilde{B}^x u^\tau - \tau \tilde{E}^\eta u^y + \tau \tilde{E}^y u^\eta \right), \\ J^y &= n u^y + d^y + \sigma \left(\tilde{E}^y u^\tau - \tau \tilde{B}^\eta u^x + \tau \tilde{B}^x u^\eta \right) \\ &\quad + \sigma_\chi \left(\tilde{B}^y u^\tau + \tau \tilde{E}^\eta u^x - \tau \tilde{E}^x u^\eta \right), \\ J^\eta &= n u^\eta + d^\eta + \sigma \left(\tilde{E}^\eta u^\tau + \frac{\tilde{B}^y}{\tau} u^x - \frac{\tilde{B}^x}{\tau} u^y \right) \\ &\quad + \sigma_\chi \left(\tilde{B}^\eta u^\tau - \frac{\tilde{E}^y}{\tau} u^x + \frac{\tilde{E}^x}{\tau} u^y \right). \end{aligned} \quad (22)$$

In order to facilitate the subsequent numerical calculations, let us further simplify the above Maxwell equations. From Eq. (18) and (19), one can get the evolution

equations of the electric and magnetic fields as,

$$\begin{aligned}\partial_x \tilde{E}^x + \partial_y \tilde{E}^y + \partial_\eta \tilde{E}^\eta &= J^\tau, \\ \partial_\tau(\tau \tilde{E}^x) &= \partial_y(\tau^2 \tilde{B}^\eta) - \partial_\eta \tilde{B}^y - \tau J^x, \\ \partial_\tau(\tau \tilde{E}^y) &= -\partial_x(\tau^2 \tilde{B}^\eta) + \partial_\eta \tilde{B}^x - \tau J^y, \\ \partial_\tau(\tau \tilde{E}^\eta) &= \partial_x \tilde{B}^y - \partial_y \tilde{B}^x - \tau J^\eta.\end{aligned}\quad (23)$$

$$\begin{aligned}\partial_x \tilde{B}^x + \partial_y \tilde{B}^y + \partial_\eta \tilde{B}^\eta &= 0, \\ \partial_\tau(\tau \tilde{B}^x) &= -\partial_y(\tau^2 \tilde{E}^\eta) + \partial_\eta \tilde{E}^y, \\ \partial_\tau(\tau \tilde{B}^y) &= \partial_x(\tau^2 \tilde{E}^\eta) - \partial_\eta \tilde{E}^x, \\ \partial_\tau(\tau \tilde{B}^\eta) &= -\partial_x \tilde{E}^y + \partial_y \tilde{E}^x.\end{aligned}\quad (24)$$

Now we can carry out the simulations with above equations (23) and (24), according to the aforementioned numerical method in Section II B. In final numerical results, we will compute the electric and magnetic field in Minkowski coordinates, which are Lorentz transformation of electric and magnetic field in Milne coordinate by the following,

$$\begin{aligned}E^x &= \cosh \eta \tilde{E}^x + \sinh \eta \tilde{B}^y, \\ E^y &= \cosh \eta \tilde{E}^y - \sinh \eta \tilde{B}^x, \\ E^z &= \tau \tilde{E}^\eta, \\ B^x &= \cosh \eta \tilde{B}^x - \sinh \eta \tilde{E}^y, \\ B^y &= \cosh \eta \tilde{B}^y + \sinh \eta \tilde{E}^x, \\ B^z &= \tau \tilde{B}^\eta.\end{aligned}\quad (25)$$

B. Electric Conductivity

The electric conductivity of QGP remains to be an open question. There are many works focusing on the electric conductivity in the hydro stage of QGP with theoretical calculations and simulations, but significantly different results are obtained. Here we briefly outline some of them in the following for further estimation of the reasonable region. First, results from different lattice QCD calculations can be different by an order of magnitude. They are listed as follows,

$$[16] \quad \frac{\sigma}{T} |_{1.5 < T/T_c < 3} = 7C_{em} \approx 0.428,$$

$$[17] \quad \frac{\sigma}{T} |_{T/T_c \approx 1.5} = (0.4 \pm 0.1)C_{em} = 0.0245 \pm 0.006,$$

$$[18, 19] \quad \begin{aligned}\frac{\sigma}{T} |_{1.1T_c} &= (0.201 \sim 0.703)C_{em} \approx (1.23 \sim 4.30) \times 10^{-2}, \\ \frac{\sigma}{T} |_{1.3T_c} &= (0.203 \sim 0.388)C_{em} \approx (1.24 \sim 2.37) \times 10^{-2}, \\ \frac{\sigma}{T} |_{1.5T_c} &= (0.218 \sim 0.413)C_{em} \approx (1.33 \sim 2.52) \times 10^{-2},\end{aligned}$$

where the factor $C_{em} = \sum_f e_f^2 \approx 0.06115$ for three-flavor case, e_f is the charge of quark with flavor f .

Additionally, results from different theoretical calculations are also different. The hard thermal loop (HTL) calculation up to leading-log for high temperature QGP produces that $\sigma/T = 11.8687 e^{\frac{\text{Tr}_f(Q_e Q_V)}{g^4 \ln(1/g)}} = 146.33(26.12)$ for

$\alpha_s = 0.01(0.05)$ [22], where $Q_e = (2/3, -1/3, -1/3)$ for (u, d, s) and the numerical results is for $Q_V = Q_e$. Meanwhile, the leading order perturbative QCD calculation gives that $\sigma/T \approx 5.98$ [28], whereas the dilute instanton-liquid model gives that $\sigma/T \approx (0.46 \sim 1.39)C_{em} \approx (0.0281 \sim 0.0850)$ [26]. The transport model with relaxation time gives us an analytical representation, (see e.g., [24, 41–44])

$$\sigma = \sum_{f,\pm} \frac{g_f q_f^2 \tau_q}{6\pi^2 T} \int \frac{k^2 dk}{E_{k,f}^2} \frac{e^{-\frac{E_{k,f} \pm \mu}{T}}}{(e^{-\frac{E_{k,f} \pm \mu}{T}} + 1)^2}, \quad (26)$$

where $+$ ($-$) sign is taken for fermion(antifermion). One can estimate $\sigma/T = 0.007 \sim 0.026$ for $T = T_c - 5T_c$ with zero chemical potential². Furthermore, the parton-hadron-string dynamics (PHSD) transport [27] approach finds that $\sigma/T \approx 0.0009 + 0.015(T - T_c)/T_c$. Finally, the microscopic relativistic transport model Boltzmann Approach to Multi-Parton Scatterings (BAMPS) simulation [45] obtained $\sigma/T \approx (0.05 \sim 0.2)$.

Based on above summary, we choose $\sigma/T = 0.1$ as a relatively reasonable value in our numerical simulation. We also take $\sigma/T = 100$ to explore the medium response in the large conductivity limit.

C. Numerical results

In this subsection, we present the simulate results of the electromagnetic field evolution in the non-static QGP. As mentioned before, the evolution of the medium formed in the relativistic heavy-ion collision, as well as that of the electromagnetic field, consists of three stages — initial ($\tau < 0.1$ fm), pre-equilibrium ($0.1 \leq \tau < 0.4$ fm), and hydro ($\tau \geq 0.4$ fm) stage. Our simulation will be arranged accordingly. The initial condition of the electromagnetic field is generated by two heavy nuclei moving toward each other. Then we solve the Maxwell's equations (23) and (24) and simulate the electromagnetic field evolution in the pre-equilibrium and stage. In the pre-equilibrium stage, the QGP is assumed to expand as a Bjorken flow, and we explore three different models for the time dependence of the electrical conductivity. Whereas in the hydro stage, we take hydro background from Bjorken flow, Gubser flow, and realistic hydro profile from the MUSIC package [46–49]. the corresponding temperature and fluid velocity are produced by these three models. (See the Appendix D for analytical forms

² In this estimation, the relaxation time is $\tau_q = \frac{1}{5.1T\alpha_s^2 \ln(\alpha_s^{-1})(1+0.12(2N_f+1))}$, $g_f = 2 \times 3$, the mass taking the effective mass composed of the bare mass and thermal mass, and the coupling constant $\alpha_s(T) = \frac{6\pi}{(33-2N_f) \ln(T/\Lambda_T)} \left(1 - \frac{3(153-19N_f) \ln(2 \ln(T/\Lambda_T))}{(33-2N_f)^2 \ln(T/\Lambda_T)}\right)$, with $\Lambda_T = 200$ MeV.

of temperature and fluid velocity in the Bjorken and Gubser solutions.) These temperature and fluid velocity profile and then read into the program and provide the background field to solve Maxwell's equations (23) and (24). In what follows, we will focus on the dynamical magnetic field at the center of the fireball [$\mathbf{x} = (0, 0, 0)$]³. Herein, we focus on the case that the net number density (n) and the diffusive current density (d^μ) are set to zero, and their influence on the dynamic evolution of the magnetic field will be studied in our future work.

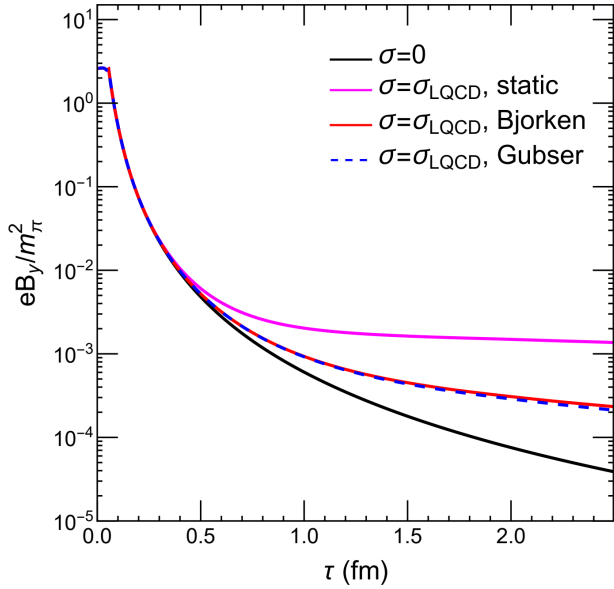


FIG. 3. The suppression effect of the longitudinal expansion of the medium.

1. suppression effect due to the longitudinal expansion of the medium

We first study the evolution of magnetic field along the out-of-plane direction (eB_y) with three different backgrounds — a static medium, Bjorken flow, and Gubser flow. We take identical electric conductivity in these three different cases, i.e., $\sigma = 0$ for the initial stage, and $\sigma = \sigma_{\text{LQCD}}$ for the pre-equilibrium and hydro stage. Results are shown in Fig. 3. We observe a suppression effect for the longitudinal expansion of the medium. The dynamical magnetic field was depressed in the Bjorken expansion and the Gubser expansion compared to the static case.

The reason of the suppression effect is illustrated in Fig. 4 and explained as follows. At the presence of a

external magnetic field along the y -axis, in-medium particles with positive(negative) at forward rapidity experience a Lorentz pointing at the negative(positive) x -direction, and vice versa for particles at backward rapidity. Collective motion of the charged particles, due to the Lorentz force, induces a clockwise circular current. It generates an induced magnetic field in the negative y -direction and thereby weakens the external magnetic field.

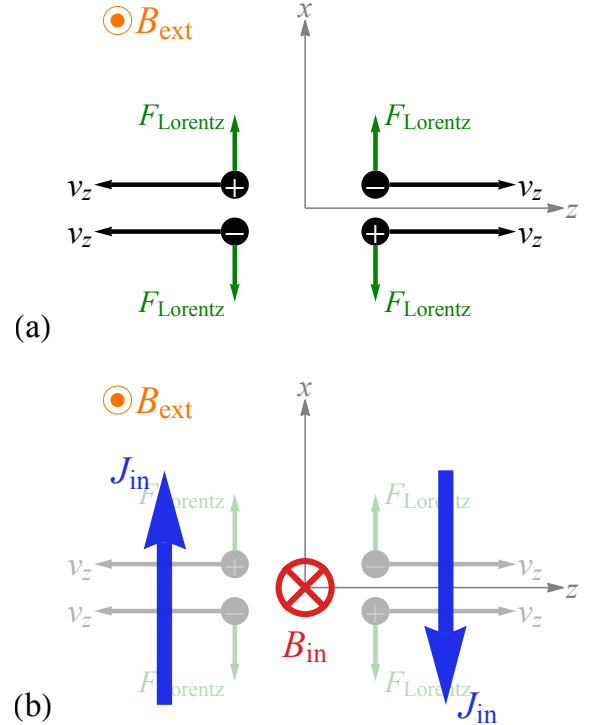


FIG. 4. Illustration of the suppression effect. (a) Lorentz force acting on in-medium charged particles due to the external magnetic field. (b) Induced electric currents due to the Lorentz force and their resulting induced magnetic field.

2. The dynamical magnetic field with realistic hydro background

Then we move on to realistic hydrodynamic background provided by numerical simulation using the MUSIC package [46–49]. We set $\sigma = 0$ at the initial stage, and we explore the medium responses to the magnetic field by choosing three different electric conductivity models in the pre-equilibrium stage and respectively setting the electric conductivity $\sigma = 0.1 T$, $\sigma = \sigma_{\text{LQCD}}$, and $\sigma = 100 T$ in the hydro stage. The three models for the pre-equilibrium stage are taken: (a) zero model that assumes vanishing conductivity, $\sigma(\tau, \mathbf{x}) = 0$; (b) constant model that assumes constant conductivity which takes the value at the initial time of hydro, $\sigma(\tau, \mathbf{x}) = \sigma(\tau = 0.4 \text{ fm}, \mathbf{x})$; and (c) linear model that the conduc-

³ It is worth noting that we can generate the dynamic magnetic and electric fields at any given coordinate and the spatial distribution of electromagnetic fields at any time under our framework.

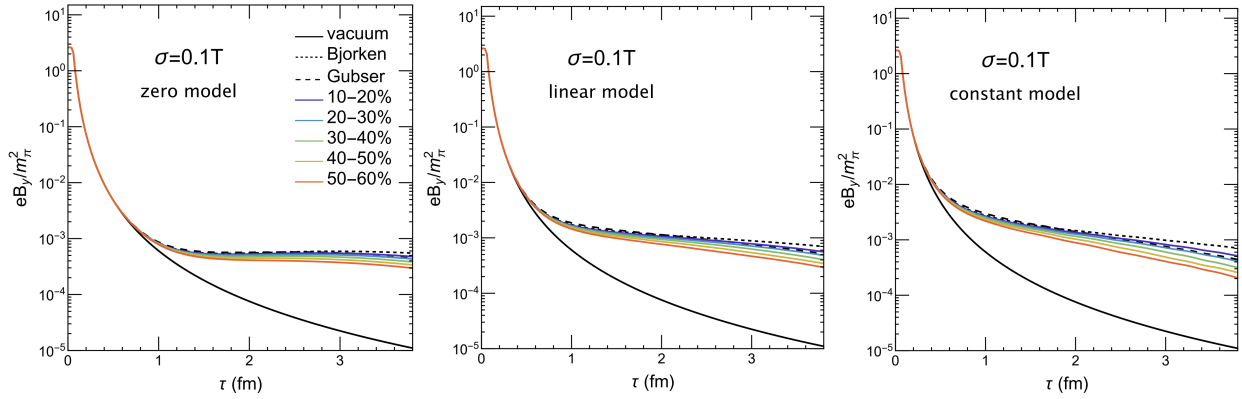


FIG. 5. Proper dependence of magnetic field along the out-of-plane direction at the center ($x = 0, y = 0, z = 0$) and with conductivity $\sigma = 0.1T$ in the hydro stage. From left to right correspond to zero, linear, and constant models for the pre-equilibrium stage. Black solid curves represent the vacuum value, whereas dotted(dashed) curves take Bjorken(Gubser) flow as the background. Colored solid curves from purple to red are respectively for realistic hydro background in the 10 – 20% to 50 – 60% centrality classes.

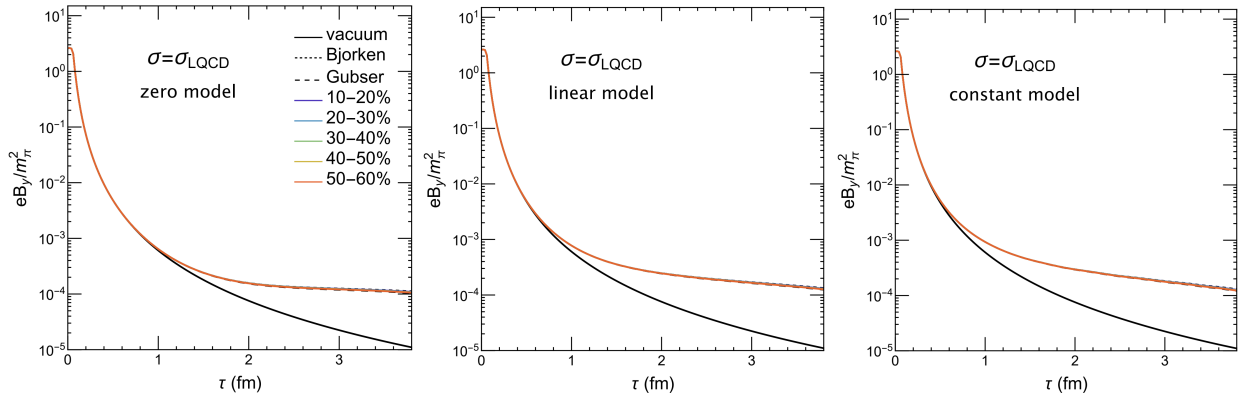


FIG. 6. Same as Fig. 5 but with hydro constant conductivity $\sigma = \sigma_{\text{LQCD}}$.

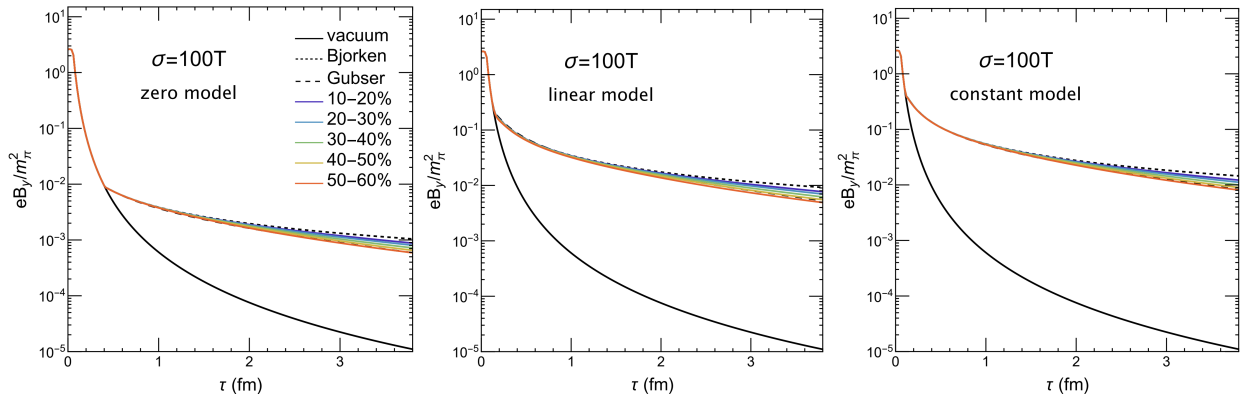


FIG. 7. Same as Fig. 5 but with hydro conductivity $\sigma = 100T$.

tivity that grows linearly from zero to the value at the hydro initial time, $\sigma(\tau, \mathbf{x}) = (\tau/0.4\text{fm})\sigma(\tau = 0.4\text{fm}, \mathbf{x})$. We will assume that the temperature and velocity of the background flow in the pre-equilibrium stage follow the Bjorken flow.

Initial conditions of both hydro and electromagnetic

field are generated by event-averaged MC-Glauber simulation for $\sqrt{s_{\text{NN}}} = 200$ GeV AuAu collisions. For a more direct comparison of the response of different hydro profiles, we fix the magnetic field to be the one with impact parameter $b = 6$ fm, and vary the hydro background from 10 – 20% to 50 – 60% centrality classes.

| | a_0 | b_0 | b_1 | b_2 | c_0 | c_1 | c_2 | c_3 |
|----------------|---------|---------|----------|---------|-------|---------|---------|--------|
| zero model | -8.848 | -2.193 | 0.412 | -0.207 | 0.0 | 13.074 | -11.66 | 19.679 |
| constant model | -21.693 | -28.039 | -148.773 | -16.302 | 0. | 159.619 | 6.285 | 4.948 |
| linear model | -10.177 | -7.549 | 0.183 | -0.299 | 0.351 | 36.926 | -16.311 | 3.285 |

TABLE I. The fit parameters of the fitted magnetic field Eq. (27) for electric conductivity $\sigma = 0.1T$ in hydro stage with different conductivity model in pre-equilibrium stage.

| | a_0 | b_0 | b_1 | b_2 | c_0 | c_1 | c_2 | c_3 |
|----------------|---------|--------|--------|--------|-------|--------|--------|---------|
| zero model | -9.924 | -2.145 | -8.568 | 3.602 | 0. | 14.76 | 12.063 | 14.417 |
| constant model | -10.871 | -1.786 | -5.669 | -7.969 | 0.0 | 10.273 | 16.761 | 20.953 |
| linear model | -10.298 | -2.785 | -6.329 | -1.854 | 0.0 | 16.528 | 10.082 | 18.5673 |

TABLE II. Same as Table. I but for constant conductivity $\sigma = \sigma_{\text{LQCD}}$.

| | a_0 | b_0 | b_1 | b_2 | c_0 | c_1 | c_2 | c_3 |
|----------------|---------|--------|--------|---------|-------|--------|--------|--------|
| zero model | -10.676 | -4.081 | -0.93 | -18.58 | 0.052 | 19.787 | 13.497 | 14.866 |
| constant model | -5.633 | -1.344 | -4.912 | 1.406 | 0. | 12.345 | -0.039 | 0.677 |
| linear model | -7.311 | -1.248 | 0.483 | -12.433 | 0. | 8.03 | -0.223 | 16.904 |

TABLE III. Same as Table. I but for conductivity $\sigma = 100T$.

Results for $\sigma = 0.1T$ in the hydro stage are presented in Fig. 5. The dynamical magnetic field is more sensitive to the electric conductivity model of the pre-equilibrium stage than to the hydro background. The dynamical magnetic fields in Bjorken, Gubser, and realistic backgrounds are almost the same except for the late time region where the magnetic field strength is very small. It means that the evolution of the y component of the magnetic field is dominated by the longitudinal expansion of the QGP, rather than the transverse expansion. We fit the magnetic field as a function of time with a parameterized function,

$$e B^y = e B_{\tau=0}^y \text{Exp} \left[a_0 e^{\frac{b_0 + b_1 \tau + b_2 \tau^2}{c_0 + c_1 \tau + c_2 \tau^2 + c_3 \tau^3}} \right]. \quad (27)$$

Corresponding parameters in Table I are fit from the data of the MUSIC hydro background with centrality 40–50%.

Then we investigate the evolution of magnetic field with the constant conductivity $\sigma = \sigma_{\text{LQCD}}$ in the hydro stage. Results are presented in Fig. 6 and parameter fit for 40–50% centrality range is listed in Table II. Given the constant conductivity, the influence of transverse expansion become negligible.

Finally, let us explore the response of a highly conductive plasma where the electric conductivity with 1000 times in the hydro stage, i.e., $\sigma = 100T$. Results are shown in Fig. 7 and Table. III. Compared with the results in Fig. 5, the late-time strength of the magnetic field is much greater, and it is more explicitly dependent on the choice of the conductivity model in the pre-equilibrium stage.

IV. CONCLUSION

To conclude, we have developed a framework to numerically simulate the dynamical magnetic fields in heavy ion

collisions. This framework has allowed us to investigate the in-medium evolution of space-time-dependent magnetic fields on top of a variety of background medium evolution models for different scenarios of electric conductivities both in the thermal phase and in the pre-equilibrium stage. Our main findings can be summarized as follows.

- In the case of a static QGP, previous results assuming constant electric conductivity are reproduced and new results with more realistic space-time-dependent electric conductivity are obtained, demonstrating a robust medium response that extends the lifetime of the magnitude and that is sensitive to the values of the conductivity.
- For an expanding QGP, we find a strong influence of the longitudinal expansion which considerably reduces the contributions from medium response and as a result leads to a much smaller magnetic fields as compared with the static case. On the other hand, the inclusion of transverse expansion in addition to the longitudinal expansion only affects the dynamical field evolution rather mildly.
- The lifetime of the dynamical magnetic fields is strongly dependent on the medium conductivities in the thermal QGP. Choosing a conductivity value in the range implied by relevant lattice simulations would only lead to a limited medium enhancement of late time field strength.
- More importantly, the lifetime is found to be particularly sensitive to, and mainly determined by, the non-equilibrium contribution from the early time partonic medium, as demonstrated by comparisons among the three different choices (zero model, constant model and linear model). A considerable pre-

hydro effective conductivity could significantly enhance the dynamical field strength.

Clearly, the main “bottleneck” for an accurate description of the dynamical magnetic fields is a better estimate of the effective conductivity for the pre-equilibrium stage, which in turn relies on a detailed understanding of the pre-thermal evolution (— especially that of the quarks and antiquarks). From a phenomenological perspective, a magnetic field lifetime on the order of ~ 1 fm/c in $\sqrt{s_{\text{NN}}} = 200$ GeV collisions appears needed for explaining relevant observables of chiral magnetic effect and the $\Lambda/\bar{\Lambda}$ global polarization splitting [50–55]. According to our findings in this work, such a lifetime would suggest a considerable medium response contribution at the very early stage of the collisions. Whether this scenario could realistically occur will be an important question for future investigation.

Finally, while this work focuses on $\sqrt{s_{\text{NN}}} = 200$ GeV Au+Au collisions, our framework can be readily applied for other colliding systems at different collision energies. The simulation code for the static case has been made available at <https://github.com/brangja/EB-in-HIC.git> and efforts are underway to make the full dynamical package publicly available in the future. Such

a framework will allow quantitative estimates of many interesting observables induced by the dynamical magnetic fields in heavy ion collisions.

ACKNOWLEDGMENTS

The authors thank Dmitri E. Kharzeev for very helpful discussions at the early stage of this work. The research of AH is supported in part by the Fundamental Research Funds for the Central Universities No. E2E46304. AH and MH are supported by the Strategic Priority Research Program of Chinese Academy of Sciences Grant No. XDB34030000, the Fundamental Research Funds for the Central Universities, and the National Natural Science Foundation of China (NSFC) Grant Nos. 12235016. MH is also supported in part by the National Natural Science Foundation of China (NSFC) Grant Nos. 11725523, 11735007, and 12221005. DS is grateful to support by Key Laboratory of Quark and Lepton Physics Contracts No. QLPL2022P01. JL acknowledges partial support by NSF Grant No. PHY-2209183 and DOE-funded Beam Energy Scan Theory (BEST) Collaboration. SS is supported by the U.S. Department of Energy, Office of Science, Office of Nuclear Physics, Grants Nos. DE-FG88ER41450 and DE-SC0012704.

Appendix A: The solutions of Eq.(11)

As mentioned before, we do not need to solve the Eq.(11), it can be represented analytically by a boosted point charge. If we choose the distribution of protons both in projectile and target according to the Woods-Saxon distribution with the standard parameters[56].

$$\rho(r) = \rho_0 \frac{1 + w \left(\frac{r}{R}\right)^2}{1 + e^{\frac{r-R}{a}}}. \quad (\text{A1})$$

To Au nucleus, $a = 0.535$ fm, $R = 6.38$ fm, $w = 0$. In this work, we will use the Gauss theorem in the rest frame of the target, and then boost the electromagnetic fields to the lab frame with the velocity of the target. In the rest frame of the target,

$$\mathbf{E}_0 = \frac{e}{4\pi} Q(r_0) \frac{\mathbf{r}_0}{r_0^3}, \quad Q(r) = 4\pi \int_0^r \rho(x) x^2 dx, \quad \mathbf{B}_0 = 0, \quad \mathbf{r}_0 = \mathbf{x} - \mathbf{x}'. \quad (\text{A2})$$

Where \mathbf{x} and \mathbf{x}' are the location of the field and nucleus center respectively. After boosting to the lab frame,

$$\begin{aligned} E_x &= \gamma E_x^0, & E_y &= \gamma E_y^0, & E_z &= E_z^0, \\ B_x &= -\gamma v E_y^0, & B_y &= \gamma v E_x^0, & B_z &= 0. \end{aligned} \quad (\text{A3})$$

The corresponding coordinates represented by the lab frame are

$$r_{0,x} = x - x', \quad r_{0,y} = y - y', \quad r_{0,z} = \gamma(z - z' - vt)$$

One can also generate the electromagnetic fields of heavy-ion collisions by using the Monte Carlo method like the work of Deng and Huang [5]. In this work, we will use the above method for simplicity.

Appendix B: The algorithm of Yee-grid method to Eq. (12)

The Yee-grid algorithm of Eq. (12) can be easily understood by the following representation,

$$\begin{aligned}
\frac{dE_x}{dt}(t + dt/2, x + dx/2, y, z) &= \left[\partial_y B_z - \partial_z B_y - \sigma E_x - \sigma_\chi B_x - \tilde{J}_x \right] | (t + dt/2, x + dx/2, y, z), \\
\frac{dE_y}{dt}(t + dt/2, x, y + dy/2, z) &= \left[\partial_z B_x - \partial_x B_z - \sigma E_y - \sigma_\chi B_y - \tilde{J}_y \right] | (t + dt/2, x, y + dy/2, z), \\
\frac{dE_z}{dt}(t + dt/2, x, y, z + dz/2) &= \left[\partial_x B_y - \partial_y B_x - \sigma E_z - \sigma_\chi B_z - \tilde{J}_z \right] | (t + dt/2, x, y, z + dz/2), \\
\frac{dB_x}{dt}(t, x, y + dy/2, z + dz/2) &= [\partial_z E_y - \partial_y E_z] | (t, x, y + dy/2, z + dz/2), \\
\frac{dB_y}{dt}(t, x + dx/2, y, z + dz/2) &= [\partial_x E_z - \partial_z E_x] | (t, x + dx/2, y, z + dz/2), \\
\frac{dB_z}{dt}(t, x + dx/2, y + dy/2, z) &= [\partial_y E_x - \partial_x E_y] | (t, x + dx/2, y + dy/2, z).
\end{aligned} \tag{B1}$$

Let us use the center difference method at the given points to solve these equations. One can get the following results,

$$\begin{aligned}
E_x|_{i+1/2,j,k}^{n+1} &= E_x|_{i+1/2,j,k}^n + dt \frac{B_z|_{i+1/2,j+1/2,k}^{n+1/2} - B_z|_{i+1/2,j-1/2,k}^{n+1/2}}{dy} - dt \frac{B_y|_{i+1/2,j,k+1/2}^{n+1/2} - B_y|_{i+1/2,j,k-1/2}^{n+1/2}}{dz} \\
&\quad - dt \left\{ \sigma E_x|_{i+1/2,j,k}^{n+1/2} + \sigma_\chi B_x|_{i+1/2,j,k}^{n+1/2} + \tilde{J}_x|_{i+1/2,j,k}^{n+1/2} \right\}, \\
E_y|_{i,j+1/2,k}^{n+1} &= E_y|_{i,j+1/2,k}^n + dt \frac{B_x|_{i,j+1/2,k+1/2}^{n+1/2} - B_x|_{i,j+1/2,k-1/2}^{n+1/2}}{dz} - dt \frac{B_z|_{i+1/2,j+1/2,k}^{n+1/2} - B_z|_{i-1/2,j+1/2,k}^{n+1/2}}{dx} \\
&\quad - dt \left\{ \sigma E_y|_{i,j+1/2,k}^{n+1/2} + \sigma_\chi B_y|_{i,j+1/2,k}^{n+1/2} + \tilde{J}_y|_{i,j+1/2,k}^{n+1/2} \right\}, \\
E_z|_{i,j,k+1/2}^{n+1} &= E_z|_{i,j,k+1/2}^n + dt \frac{B_y|_{i+1/2,j,k+1/2}^{n+1/2} - B_y|_{i-1/2,j,k+1/2}^{n+1/2}}{dx} - dt \frac{B_x|_{i,j+1/2,k+1/2}^{n+1/2} - B_x|_{i,j-1/2,k+1/2}^{n+1/2}}{dy} \\
&\quad - dt \left\{ \sigma E_z|_{i,j,k+1/2}^{n+1/2} + \sigma_\chi B_z|_{i,j,k+1/2}^{n+1/2} + \tilde{J}_z|_{i,j,k+1/2}^{n+1/2} \right\}.
\end{aligned} \tag{B2}$$

$$\begin{aligned}
B_x|_{i,j+1/2,k+1/2}^{n+1/2} &= B_x|_{i,j+1/2,k+1/2}^{n-1/2} + dt \left\{ \frac{E_y|_{i,j+1/2,k+1}^n - E_y|_{i,j+1/2,k}^n}{dz} - \frac{E_z|_{i,j+1,k+1/2}^n - E_z|_{i,j,k+1/2}^n}{dy} \right\}, \\
B_y|_{i+1/2,j,k+1/2}^{n+1/2} &= B_y|_{i+1/2,j,k+1/2}^{n-1/2} + dt \left\{ \frac{E_z|_{i+1,j,k+1/2}^n - E_z|_{i,j,k+1/2}^n}{dx} - \frac{E_x|_{i+1/2,j+1,k+1}^n - E_x|_{i+1/2,j,k}^n}{dz} \right\}, \\
B_z|_{i+1/2,j+1/2,k}^{n+1/2} &= B_z|_{i+1/2,j+1/2,k}^{n-1/2} + dt \left\{ \frac{E_x|_{i+1/2,j+1,k}^n - E_x|_{i+1/2,j,k}^n}{dy} - \frac{E_y|_{i+1,j+1/2,k}^n - E_y|_{i,j+1/2,k}^n}{dx} \right\}.
\end{aligned} \tag{B3}$$

These two sets of equations should be further simplified for the next numerical simulations. Then the electric parts can be cast into the following,

$$\begin{aligned}
E_x|_{i+1/2,j,k}^{n+1} &= COE|_{i+1/2,j,k}^{n+1/2} E_x|_{i+1/2,j,k}^n + CE|_{i+1/2,j,k}^{n+1/2} \left[\frac{dt}{dy} \left(B_z|_{i+1/2,j+1/2,k}^{n+1/2} - B_z|_{i+1/2,j-1/2,k}^{n+1/2} \right) \right. \\
&\quad \left. - \frac{dt}{dz} \left(B_y|_{i+1/2,j,k+1/2}^{n+1/2} - B_y|_{i+1/2,j,k-1/2}^{n+1/2} \right) - dt \sigma_\chi|_{i+1/2,j,k}^{n+1/2} B_x|_{i+1/2,j,k}^{n+1/2} - dt \tilde{J}_x|_{i+1/2,j,k}^{n+1/2} \right] \\
E_y|_{i,j+1/2,k}^{n+1} &= COE|_{i,j+1/2,k}^{n+1/2} E_y|_{i,j+1/2,k}^n + CE|_{i,j+1/2,k}^{n+1/2} \left[\frac{dt}{dz} \left(B_x|_{i,j+1/2,k+1/2}^{n+1/2} - B_x|_{i,j+1/2,k-1/2}^{n+1/2} \right) \right. \\
&\quad \left. - \frac{dt}{dx} \left(B_z|_{i+1/2,j+1/2,k}^{n+1/2} - B_z|_{i-1/2,j+1/2,k}^{n+1/2} \right) - dt \sigma_\chi|_{i,j+1/2,k}^{n+1/2} B_y|_{i,j+1/2,k}^{n+1/2} - dt \tilde{J}_y|_{i,j+1/2,k}^{n+1/2} \right] \\
E_z|_{i,j,k+1/2}^{n+1} &= COE|_{i,j,k+1/2}^{n+1/2} E_z|_{i,j,k+1/2}^n + CE|_{i,j,k+1/2}^{n+1/2} \left[\frac{dt}{dx} \left(B_y|_{i+1/2,j,k+1/2}^{n+1/2} - B_y|_{i-1/2,j,k+1/2}^{n+1/2} \right) \right. \\
&\quad \left. - \frac{dt}{dy} \left(B_x|_{i,j+1/2,k+1/2}^{n+1/2} - B_x|_{i,j-1/2,k+1/2}^{n+1/2} \right) - dt \sigma_\chi|_{i,j,k+1/2}^{n+1/2} B_z|_{i,j,k+1/2}^{n+1/2} - dt \tilde{J}_z|_{i,j,k+1/2}^{n+1/2} \right]
\end{aligned} \tag{B4}$$

Where we have used an approximation $E_i|^{n+1/2} = (E_i|^{n+1} + E_i|^{n+1/2})/2$ for the term σE_i , herein $i = x, y, z$.

While the magnetic field parts can be written as,

$$\begin{aligned}
B_x|_{i,j+1/2,k+1/2}^{n+1/2} &= B_x|_{i,j+1/2,k+1/2}^{n-1/2} + \frac{dt}{dz} \left(E_y|_{i,j+1/2,k+1}^n - E_y|_{i,j+1/2,k}^n \right) \\
&\quad - \frac{dt}{dy} \left(E_z|_{i,j+1,k+1/2}^n - E_z|_{i,j,k+1/2}^n \right) \\
B_y|_{i+1/2,j,k+1/2}^{n+1/2} &= B_y|_{i+1/2,j,k+1/2}^{n-1/2} + \frac{dt}{dx} \left(E_z|_{i+1,j,k+1/2}^n - E_z|_{i,j,k+1/2}^n \right) \\
&\quad - \frac{dt}{dz} \left(E_x|_{i+1/2,j,k+1}^n - E_x|_{i+1/2,j,k}^n \right) \\
B_z|_{i+1/2,j+1/2,k}^{n+1/2} &= B_z|_{i+1/2,j+1/2,k}^{n-1/2} + \frac{dt}{dy} \left(E_x|_{i+1/2,j+1,k}^n - E_x|_{i+1/2,j,k}^n \right) \\
&\quad - \frac{dt}{dx} \left(E_y|_{i+1,j+1/2,k}^n - E_y|_{i,j+1/2,k}^n \right)
\end{aligned} \tag{B5}$$

Firstly, the corresponding coordinates (n, i, j, k) denotes $(t_0 + n dt, x_0 + i dx, y_0 + j dy, z_0 + k dz)$, herein $n, i, j, k = 0, 1, 2, \dots$. And the coefficients

$$CE|_{i,j,k}^n = \frac{2}{2 + dt \sigma|_{i,j,k}^n}, \quad COE|_{i,j,k}^n = \frac{2 - dt \sigma|_{i,j,k}^n}{2 + dt \sigma|_{i,j,k}^n}. \tag{B6}$$

In which $\sigma|_{i,j,k}^n = \sigma(t_0 + n dt, x_0 + i dx, y_0 + j dy, z_0 + k dz)$.

Secondly, the external source terms,

$$\tilde{J}_m|_{i,j,k}^n = \sigma|_{i,j,k}^n E_m^{ext}|_{i,j,k}^n + \sigma_\chi|_{i,j,k}^n B_m^{ext}|_{i,j,k}^n, \quad m = (x, y, z). \tag{B7}$$

Finally, the coordinates of the magnetic field at the last second term in each equation of the set of equations (B4) is not located at the same position of the computing magnetic field. So we need to represent it with the computing magnetic field. There is one method to solve this problem, i.e

$$\begin{aligned}
B_x|_{i+1/2,j,k}^{n+1/2} &= \frac{1}{8} \left(B_x|_{i+1,j+1/2,k+1/2}^{n+1/2} + B_x|_{i+1,j+1/2,k-1/2}^{n+1/2} + B_x|_{i+1,j-1/2,k+1/2}^{n+1/2} + B_x|_{i+1,j-1/2,k-1/2}^{n+1/2} \right. \\
&\quad \left. B_x|_{i,j+1/2,k+1/2}^{n+1/2} + B_x|_{i,j+1/2,k-1/2}^{n+1/2} + B_x|_{i,j-1/2,k+1/2}^{n+1/2} + B_x|_{i,j-1/2,k-1/2}^{n+1/2} \right), \\
B_y|_{i,j+1/2,k}^{n+1/2} &= \frac{1}{8} \left(B_y|_{i+1/2,j+1,k+1/2}^{n+1/2} + B_y|_{i+1/2,j+1,k-1/2}^{n+1/2} + B_y|_{i-1/2,j+1,k+1/2}^{n+1/2} + B_y|_{i-1/2,j+1,k-1/2}^{n+1/2} \right. \\
&\quad \left. B_y|_{i+1/2,j,k+1/2}^{n+1/2} + B_y|_{i+1/2,j,k-1/2}^{n+1/2} + B_y|_{i-1/2,j,k+1/2}^{n+1/2} + B_y|_{i-1/2,j,k-1/2}^{n+1/2} \right), \\
B_z|_{i,j,k+1/2}^{n+1/2} &= \frac{1}{8} \left(B_z|_{i+1/2,j+1/2,k+1}^{n+1/2} + B_z|_{i+1/2,j-1/2,k+1}^{n+1/2} + B_z|_{i-1/2,j+1/2,k+1}^{n+1/2} + B_z|_{i-1/2,j-1/2,k+1}^{n+1/2} \right. \\
&\quad \left. B_z|_{i+1/2,j+1/2,k}^{n+1/2} + B_z|_{i+1/2,j-1/2,k}^{n+1/2} + B_z|_{i-1/2,j+1/2,k}^{n+1/2} + B_z|_{i-1/2,j-1/2,k}^{n+1/2} \right),
\end{aligned} \tag{B8}$$

Appendix C: Levi-Civita tensor and electromagnetic tensor in Milne space

In Milne coordinate, the Levi-Civita tensor is different from those in the Minkowski coordinate,

$$\epsilon^{\mu\nu\rho\sigma} = \frac{1}{\sqrt{|g|}} \tilde{\epsilon}^{\mu\nu\rho\sigma}, \quad \epsilon_{\mu\nu\rho\sigma} = \theta(g) \sqrt{|g|} \tilde{\epsilon}_{\mu\nu\rho\sigma}, \tag{C1}$$

where $g = \det(g_{\mu\nu})$, θ is the Heaviside step function, and the Levi-Civita symbol in the Minkowski coordinate $\tilde{\epsilon}^{\mu\nu\rho\sigma}$ is defined by the following,

$$\tilde{\epsilon}^{\mu\nu\rho\sigma} = \tilde{\epsilon}_{\mu\nu\rho\sigma} = \begin{cases} +1, & \text{even permutation of } (0,1,2,\dots,n-1), \\ -1, & \text{odd permutation of } (0,1,2,\dots,n-1), \\ 0, & \text{otherwise.} \end{cases}$$

Taking that $g = -\tau^2$ and $|g| = \tau^2$, one finds $\epsilon^{0123} = \frac{1}{\tau}$ and $\epsilon_{0123} = -\tau$.

The electric and magnetic fields in the Milne space are defined by the following,

$$\tilde{E}^i = F_M^{i0}, \quad \tilde{B}^i = \tilde{F}_M^{i0}. \quad (\text{C2})$$

Then one can directly derive the electromagnetic tensor in Milne space with the above Levi-Civita definition, which can be expressed as the following,

$$F_M^{\mu\nu} = \begin{pmatrix} 0 & -\tilde{E}^x & -\tilde{E}^y & -\tilde{E}^\eta \\ \tilde{E}^x & 0 & -\tau \tilde{B}^\eta & \tilde{B}^y \\ \tilde{E}^y & \tau \tilde{B}^\eta & 0 & -\tilde{B}^x \\ \tilde{E}^\eta & -\tilde{B}^y & \tilde{B}^x & 0 \end{pmatrix}, \quad \tilde{F}_M^{\mu\nu} = \begin{pmatrix} 0 & -\tilde{B}^x & -\tilde{B}^y & -\tilde{B}^\eta \\ \tilde{B}^x & 0 & \tau \tilde{E}^\eta & -\tilde{E}^y \\ \tilde{B}^y & -\tau \tilde{E}^\eta & 0 & \tilde{E}^x \\ \tilde{B}^\eta & \tilde{E}^y & -\tilde{E}^x & 0 \end{pmatrix} \quad (\text{C3})$$

Appendix D: The velocity in Milne space and Minkowski space

We will need some simplified velocities of the medium when we do the numerical calculations in the moving medium for doing comparisons, such as the static velocity, Bjorken velocity, and Gubser velocity. These velocities in the Milne space and Minkowski coordinate can be expressed as the following,

$$u_M^\mu = R^\mu_\nu u^\nu = \begin{cases} \left(\cosh \eta, 0, 0, -\frac{\sinh \eta}{\tau} \right), & \text{for static case: } u^\mu = (1, 0, 0, 0), \\ (1, 0, 0, 0), & \text{for Bjorken flow: } u^\mu = \left(\frac{t}{\tau}, 0, 0, \frac{z}{\tau} \right), \\ \left(u^\tau, u^\perp \frac{x}{x_\perp}, u^\perp \frac{y}{x_\perp}, 0 \right), & \text{for Gubser flow: } u^\mu = (u^\tau \cosh \eta, u^\perp \frac{x}{x_\perp}, u^\perp \frac{y}{x_\perp}, u^\tau \sinh \eta). \end{cases} \quad (\text{D1})$$

The velocity with M subscript represents the velocity in Milne coordinate, while the velocity without M subscript the velocity in Minkowski coordinate. The transformation matrix and anti-transformation matrix from Minkowski coordinate to Milne space are defined as follows,

$$R^\mu_\nu = \frac{\partial x_M^\mu}{\partial x^\nu} = \begin{bmatrix} \cosh \eta & 0 & 0 & -\sinh \eta \\ 0 & 1 & 0 & 0 \\ 0 & 0 & 1 & 0 \\ -\frac{\sinh \eta}{\tau} & 0 & 0 & \frac{\cosh \eta}{\tau} \end{bmatrix}, \quad \tilde{R}^\mu_\nu = \frac{\partial x^\mu}{\partial x_M^\nu} = \begin{bmatrix} \cosh \eta & 0 & 0 & \tau \sinh \eta \\ 0 & 1 & 0 & 0 \\ 0 & 0 & 1 & 0 \\ \sinh \eta & 0 & 0 & \tau \cosh \eta \end{bmatrix} \quad (\text{D2})$$

The corresponding components in the velocity of the Gubser flow are expressed as the following [57, 58],

$$u^\tau = \frac{1 + q^2 \tau^2 + q^2 x_\perp^2}{2q\tau \sqrt{1 + g^2}}, \quad u^\perp = \frac{qx_\perp}{\sqrt{1 + g^2}}, \quad g = \frac{1 + q^2 x_\perp^2 - q^2 \tau^2}{2q\tau}. \quad (\text{D3})$$

Herein the proper time is defined by $\tau = \sqrt{t^2 - z^2}$, and the transverse distance $x_\perp = \sqrt{x^2 + y^2}$. While the temperature in the local rest frame of the fluid is defined as

$$T = \frac{1}{\tau f_*^{1/4}} \left(\frac{\hat{T}_0}{(1 + g^2)^{1/3}} + \frac{H_0 g}{\sqrt{1 + g^2}} \left[1 - (1 + g^2)^{1/6} {}_2F_1 \left(\frac{1}{2}, \frac{1}{6}; \frac{3}{2}; -g^2 \right) \right] \right). \quad (\text{D4})$$

\hat{T}_0 is a dimensionless integration constant, and $f_* = \epsilon/T^4 = 11$, $q = 1/(4.3 \text{ fm})$. For RHIC energy $\sqrt{s_{\text{NN}}} = 200 \text{ GeV}$, $\hat{T}_0 = 5.55$ and $H_0 = 0.33$. The function ${}_2F_1$ denotes a hypergeometric function.

For the Bjorken flow, the temperature changes as follows,

$$T(\tau) = T_0 \frac{\tau_0}{\tau}, \quad (\text{D5})$$

where the T_0 is the temperature at time τ_0 , which can be given by the Glauber model. For example, $T_0 \sim 400 \text{ MeV}$ at the center of the QGP at $\tau_0 = 0.4 \text{ fm}$ for $\sqrt{s_{\text{NN}}} = 200 \text{ GeV}$ Au+Au collisions.

[1] Dmitri E. Kharzeev, Larry D. McLerran, and Harmen J. Warringa. The Effects of topological charge change in

heavy ion collisions: 'Event by event P and CP violation'.

- Nucl. Phys.*, A803:227–253, 2008.
- [2] V. Skokov, A. Yu. Illarionov, and V. Toneev. Estimate of the magnetic field strength in heavy-ion collisions. *Int. J. Mod. Phys. A*, 24:5925–5932, 2009.
- [3] V. Voronyuk, V. D. Toneev, W. Cassing, E. L. Bratkovskaya, V. P. Konchakovski, and S. A. Voloshin. (Electro-)Magnetic field evolution in relativistic heavy-ion collisions. *Phys. Rev.*, C83:054911, 2011.
- [4] Adam Bzdak and Vladimir Skokov. Event-by-event fluctuations of magnetic and electric fields in heavy ion collisions. *Phys. Lett. B*, 710:171–174, 2012.
- [5] Wei-Tian Deng and Xu-Guang Huang. Event-by-event generation of electromagnetic fields in heavy-ion collisions. *Phys. Rev. C*, 85:044907, 2012.
- [6] John Błoczyński, Xu-Guang Huang, Xilin Zhang, and Jinfeng Liao. Azimuthally fluctuating magnetic field and its impacts on observables in heavy-ion collisions. *Phys. Lett. B*, 718:1529–1535, 2013.
- [7] L. McLerran and V. Skokov. Comments About the Electromagnetic Field in Heavy-Ion Collisions. *Nucl. Phys.*, A929:184–190, 2014.
- [8] Kirill Tuchin. Initial value problem for magnetic fields in heavy ion collisions. *Phys. Rev. C*, 93(1):014905, 2016.
- [9] Dmitri E. Kharzeev, Karl Landsteiner, Andreas Schmitt, and Ho-Ung Yee. ‘Strongly interacting matter in magnetic fields’: an overview. *Lect. Notes Phys.*, 871:1–11, 2013.
- [10] D. E. Kharzeev, J. Liao, S. A. Voloshin, and G. Wang. Chiral magnetic and vortical effects in high-energy nuclear collisions—A status report. *Prog. Part. Nucl. Phys.*, 88:1–28, 2016.
- [11] Dmitri E. Kharzeev and Jinfeng Liao. Chiral magnetic effect reveals the topology of gauge fields in heavy-ion collisions. *Nature Rev. Phys.*, 3(1):55–63, 2021.
- [12] Kenji Fukushima. Extreme matter in electromagnetic fields and rotation. *Prog. Part. Nucl. Phys.*, 107:167–199, 2019.
- [13] Igor A. Shovkovy. Anomalous plasma: chiral magnetic effect and all that. 11 2021.
- [14] Wei Li and Gang Wang. Chiral Magnetic Effects in Nuclear Collisions. *Ann. Rev. Nucl. Part. Sci.*, 70:293–321, 2020.
- [15] Xu-Guang Huang. Electromagnetic fields and anomalous transports in heavy-ion collisions — A pedagogical review. *Rept. Prog. Phys.*, 79(7):076302, 2016.
- [16] Sourendu Gupta. The Electrical conductivity and soft photon emissivity of the QCD plasma. *Phys. Lett.*, B597:57–62, 2004.
- [17] Gert Aarts, Chris Allton, Justin Foley, Simon Hands, and Seyong Kim. Spectral functions at small energies and the electrical conductivity in hot, quenched lattice QCD. *Phys. Rev. Lett.*, 99:022002, 2007.
- [18] H. T. Ding, A. Francis, O. Kaczmarek, F. Karsch, E. Laermann, and W. Soeldner. Thermal dilepton rate and electrical conductivity: An analysis of vector current correlation functions in quenched lattice QCD. *Phys. Rev.*, D83:034504, 2011.
- [19] Heng-Tong Ding, Olaf Kaczmarek, and Florian Meyer. Thermal dilepton rates and electrical conductivity of the QGP from the lattice. *Phys. Rev.*, D94(3):034504, 2016.
- [20] Gert Aarts and J. M. Martinez Resco. Ward identity and electrical conductivity in hot QED. *JHEP*, 11:022, 2002.
- [21] Xu-Guang Huang and Jinfeng Liao. Axial Current Generation from Electric Field: Chiral Electric Separation Effect. *Phys. Rev. Lett.*, 110(23):232302, 2013.
- [22] Yin Jiang, Xu-Guang Huang, and Jinfeng Liao. Chiral electric separation effect in the quark-gluon plasma. *Phys. Rev.*, D91(4):045001, 2015.
- [23] Vishnu M. Bannur. Self-consistent quasiparticle model for quark-gluon plasma. *Phys. Rev.*, C75:044905, 2007.
- [24] Arpan Das, Hiranmaya Mishra, and Ranjita K. Mohapatra. Electrical conductivity and Hall conductivity of a hot and dense hadron gas in a magnetic field: A relaxation time approach. *Phys. Rev. D*, 99(9):094031, 2019.
- [25] A. Hosoya and K. Kajantie. Transport Coefficients of QCD Matter. *Nucl. Phys.*, B250:666–688, 1985.
- [26] Seung-il Nam. Electrical conductivity of quark matter at finite T under external magnetic field. *Phys. Rev.*, D86:033014, 2012.
- [27] W. Cassing, O. Linnyk, T. Steinert, and V. Ozvenchuk. Electrical Conductivity of Hot QCD Matter. *Phys. Rev. Lett.*, 110(18):182301, 2013.
- [28] Peter Brockway Arnold, Guy D Moore, and Laurence G. Yaffe. Transport coefficients in high temperature gauge theories. 2. Beyond leading log. *JHEP*, 05:051, 2003.
- [29] Zeyan Wang, Jiaying Zhao, Carsten Greiner, Zhe Xu, and Pengfei Zhuang. Incomplete electromagnetic response of hot QCD matter. *Phys. Rev. C*, 105(4):L041901, 2022.
- [30] Victor Roy, Shi Pu, Luciano Rezzolla, and Dirk Rischke. Analytic Bjorken flow in one-dimensional relativistic magnetohydrodynamics. *Phys. Lett. B*, 750:45–52, 2015.
- [31] Shi Pu, Victor Roy, Luciano Rezzolla, and Dirk H. Rischke. Bjorken flow in one-dimensional relativistic magnetohydrodynamics with magnetization. *Phys. Rev. D*, 93(7):074022, 2016.
- [32] Gabriele Inghirami, Luca Del Zanna, Andrea Beraudo, Mohsen Haddadi Moghaddam, Francesco Becattini, and Marcus Bleicher. Numerical magneto-hydrodynamics for relativistic nuclear collisions. *Eur. Phys. J. C*, 76(12):659, 2016.
- [33] Gabriele Inghirami, Mark Mace, Yuji Hirono, Luca Del Zanna, Dmitri E. Kharzeev, and Marcus Bleicher. Magnetic fields in heavy ion collisions: flow and charge transport. *Eur. Phys. J. C*, 80(3):293, 2020.
- [34] Umut Gürsoy, Dmitri Kharzeev, and Krishna Rajagopal. Magnetohydrodynamics, charged currents and directed flow in heavy ion collisions. *Phys. Rev.*, C89(5):054905, 2014.
- [35] Umut Gürsoy, Dmitri Kharzeev, Eric Marcus, Krishna Rajagopal, and Chun Shen. Charge-dependent Flow Induced by Magnetic and Electric Fields in Heavy Ion Collisions. *Phys. Rev.*, C98(5):055201, 2018.
- [36] Hui Li, Xin-li Sheng, and Qun Wang. Electromagnetic fields with electric and chiral magnetic conductivities in heavy ion collisions. *Phys. Rev.*, C94(4):044903, 2016.
- [37] B. G. Zakharov. Electromagnetic response of quark-gluon plasma in heavy-ion collisions. *Phys. Lett.*, B737:262–266, 2014.
- [38] Alessandro Amato, Gert Aarts, Chris Allton, Pietro Giudice, Simon Hands, and Jon-Ivar Skullerud. Transport coefficients of the QGP. *PoS, LATTICE2013*:176, 2014.
- [39] Kane Yee. Numerical solution of initial boundary value problems involving maxwell’s equations in isotropic media. *IEEE Transactions on Antennas and Propagation*, 14(3):302–307, 1966.
- [40] Dmitri E. Kharzeev and Harmen J. Warringa. Chiral Magnetic conductivity. *Phys. Rev.*, D80:034028, 2009.

- [41] Lata Thakur, P.K. Srivastava, Guru Prakash Kadam, Manu George, and Hiranmaya Mishra. Shear viscosity η to electrical conductivity σ_{el} ratio for an anisotropic QGP. *Phys. Rev. D*, 95(9):096009, 2017.
- [42] Guru Prakash Kadam, Hiranmaya Mishra, and Lata Thakur. Electrical and thermal conductivities of hot and dense hadronic matter. *Phys. Rev. D*, 98(11):114001, 2018.
- [43] Lata Thakur and P.K. Srivastava. Electrical conductivity of a hot and dense QGP medium in a magnetic field. *Phys. Rev. D*, 100(7):076016, 2019.
- [44] Arpan Das, Hiranmaya Mishra, and Ranjita K. Mohapatra. Electrical conductivity and Hall conductivity of hot and dense quark gluon plasma in a magnetic field: a quasi particle approach. *Phys. Rev.*, D101(3):034027, 2020.
- [45] Moritz Greif, Ioannis Bouras, Carsten Greiner, and Zhe Xu. Electric conductivity of the quark-gluon plasma investigated using a perturbative QCD based parton cascade. *Phys. Rev. D*, 90(9):094014, 2014.
- [46] Charles Gale, Sangyong Jeon, and Bjoern Schenke. Hydrodynamic Modeling of Heavy-Ion Collisions. *Int. J. Mod. Phys. A*, 28:1340011, 2013.
- [47] Bjorn Schenke, Sangyong Jeon, and Charles Gale. Elliptic and triangular flow in event-by-event (3+1)D viscous hydrodynamics. *Phys. Rev. Lett.*, 106:042301, 2011.
- [48] Bjoern Schenke, Sangyong Jeon, and Charles Gale. (3+1)D hydrodynamic simulation of relativistic heavy-ion collisions. *Phys. Rev. C*, 82:014903, 2010.
- [49] Scott McDonald, Chun Shen, Francois Fillion-Gourdeau, Sangyong Jeon, and Charles Gale. Hydrodynamic predictions for Pb+Pb collisions at 5.02 TeV. *Phys. Rev. C*, 95(6):064913, 2017.
- [50] Berndt Müller and Andreas Schäfer. Chiral magnetic effect and an experimental bound on the late time magnetic field strength. *Phys. Rev. D*, 98(7):071902, 2018.
- [51] Xingyu Guo, Jinfeng Liao, and Enke Wang. Spin Hydrodynamic Generation in the Charged Subatomic Swirl. *Sci. Rep.*, 10(1):2196, 2020.
- [52] Yu Guo, Shuzhe Shi, Shengqin Feng, and Jinfeng Liao. Magnetic Field Induced Polarization Difference between Hyperons and Anti-hyperons. *Phys. Lett. B*, 798:134929, 2019.
- [53] Shuzhe Shi, Yin Jiang, Elias Lilleskov, and Jinfeng Liao. Anomalous Chiral Transport in Heavy Ion Collisions from Anomalous-Viscous Fluid Dynamics. *Annals Phys.*, 394:50–72, 2018.
- [54] Shuzhe Shi, Hui Zhang, Defu Hou, and Jinfeng Liao. Signatures of Chiral Magnetic Effect in the Collisions of Isobars. *Phys. Rev. Lett.*, 125:242301, 2020.
- [55] Kun Xu, Fan Lin, Anping Huang, and Mei Huang. Λ/Λ^- polarization and splitting induced by rotation and magnetic field. *Phys. Rev. D*, 106(7):L071502, 2022.
- [56] B. Alver, M. Baker, C. Loizides, and P. Steinberg. The PHOBOS Glauber Monte Carlo. 2008.
- [57] Steven S. Gubser. Symmetry constraints on generalizations of Bjorken flow. *Phys. Rev.*, D82:085027, 2010.
- [58] Steven S. Gubser and Amos Yarom. Conformal hydrodynamics in Minkowski and de Sitter spacetimes. *Nucl. Phys.*, B846:469–511, 2011.